Research Article | Vol. 12, No. 1 / 1 January 2021 / Biomedical Optics Express 395
Biomedical Optics EXPRESS

# Hyperspectral imaging and spectral unmixing for improving whole-body fluorescence cryo-imaging

DENNIS WIRTH,[1,3] BROOK BYRD,[2,3] BOYU MENG,[2] RENDALL R. STRAWBRIDGE,[2] KIMBERLEY S. SAMKOE,[1,2] AND SCOTT C. DAVIS[2,*]

[1]*Department of Surgery, Dartmouth-Hitchcock Medical Center, 1 Medical Center Drive, Lebanon, NH 03756, USA*
[2]*Thayer School of Engineering at Dartmouth, 14 Engineering Drive, Hanover, NH 03755, USA*
[3]*Indicates equal contributions*
[*]*Scott.C.Davis@dartmouth.edu*

**Abstract:** Whole-animal fluorescence cryo-imaging is an established technique that enables visualization of the biodistribution of labeled drugs, contrast agents, functional reporters and cells in detail. However, many tissues produce endogenous autofluorescence, which can confound interpretation of the cryo-imaging volumes. We describe a multi-channel, hyperspectral cryo-imaging system that acquires densely-sampled spectra at each pixel in the 3-dimensional stack. This information enables the use of spectral unmixing to isolate the fluorophore-of-interest from autofluorescence and/or other fluorescent reporters. In phantoms and a glioma xenograft model, we show that the approach improves detection limits, increases tumor contrast, and can dramatically alter image interpretation.



## 1. Introduction

The ability to image labeled molecules or cells that inform on biological function throughout the entire body has long been a central aim of molecular imaging. This capability is important across biomedical disciplines, from studying drug candidate biodistribution and activity; tracking tumor growth and cell migration; understanding biological function using environment-sensitive reporters; and developing novel imaging agents, among other objectives [1–7]. Yet, acquiring this information at both high resolution and in large volumes is an enduring challenge. Conventional non-invasive whole-animal imaging modalities are limited in resolution and most are incapable of routinely imaging multiple reporters simultaneously. Optical techniques can provide highly-multiplexed imaging at high resolution, yet while technologies have been introduced to reveal high-fidelity subsurface information [8–15], the severe depth-resolution trade-off has limited the role of optical imaging in intact animal volumes.

In this context, whole body fluorescence cryo-imaging has emerged as an attractive technique that provides high-resolution three-dimensional fluorescent and anatomic information in whole-animal models or other tissue specimens [16–19]. This capability has been applied in a variety of capacities, including anatomic phenotyping [19,20], blood flow mapping [16,17,21,22], cellular quantification [23,24], tracking metastatic spread [25,26], and the study of contrast agent biodistribution [26,27]. Most cryo-imaging techniques employ a motorized cryo-microtome with serial slice-and-image acquisition sequences and high-resolution fluorescence imaging to create registered stacks of 2D images containing anatomic and functional information of pre-clinical small animal models [16–19]. Some systems have been developed with multiple fluorescence channels to enable multiplexed imaging of fluorophores [16,17,22,26–29].

#410810 https://doi.org/10.1364/BOE.410810
Journal © 2021 Received 25 Sep 2020; revised 13 Nov 2020; accepted 25 Nov 2020; published 16 Dec 2020

Biomedical Optics EXPRESS

A persistent challenge in applying fluorescence imaging in tissues, especially in the visible wavebands, is the contaminating effects of endogenous fluorescence [30,31]. Imaging systems that use conventional long- or band-pass emission filters are often incapable of distinguishing between endogenous fluorescence and agent-specific fluorescence signal. Depending on the relative contribution of each emitter, the endogenous signal may represent a major confounder in data interpretation. Techniques to address this problem, including time gating [32–34]. and spectral unmixing [35–39] have been used in a variety of applications. The latter of these, acquiring densely-sampled spectral data and fitting measured data to pre-recorded basis spectra, has a track record of use for epi-illumination small animal imaging [36,37] and clinical fluorescence guided surgery [40,41], frequently demonstrating significant improvements in sensitivity to the fluorophore-of-interest and thus more specific measurements. This approach can also facilitate unmixing of overlapping fluorophores during highly-multiplexed imaging. Deploying this unmixing technique in whole-body cryo-imaging could substantially improve the accuracy of reporter biodistribution. In this study, we describe and evaluate a novel multi-channel whole-body cryo-imaging system that implements hyperspectral image acquisition and accompanying processing routines to improve imaging performance. Using tissue-simulating phantoms and animal models co-administered three commonly-used fluorophores, we quantify the improvements in sensitivity to the reporters provided by spectral information, and evaluate the impact on image interpretation.

## 2. Materials and methods

### 2.1. Hyperspectral cryo-imaging instrument

The hyperspectral whole body cryo-imaging system consists of a Leica CM3600 whole animal cryo-macrotome modified with a custom-built multi-channel hyperspectral optical imaging system, as depicted in Fig. 1(A). The cryostat/macrotome unit was retrofitted with new motors, encoders and customized software control, and is capable of automatically sectioning specimens as large as 10 cm x 10 cm x 5 cm (depth) in sub-10-μm sections. The imaging system is mounted to the top of the CM3600 cabinet (Fig. 1(A) inset), suspended over the opening normally occupied by a heated viewing window and positioned to image the cut surface of the remaining specimen block after each slice is removed. The viewing window was replaced with light-opaque board configured with ports for light sources and the objective lens, the latter of which views the specimen through a surgical microscope lens cover (Carl Zeiss Meditec, Inc Dublin, CA). The small volume between the lens and cover is enclosed, though not sealed, and maintained under a slow nitrogen purge to prevent condensation.

A rendering and schematic of the optical imaging system are shown in Fig. 1(A-inset) and 1(B), respectively. This system consists of a thick aluminum mounting plate that can accommodate up to six LED's or beam expanding lenses circumscribing the objective lens. In this study, we used four light sources: A 6500 K white light LED and 470 nm LED (180 mW and 200 mW, respectively, Mightex, Toronto, ON), a 635 nm laser (250 mW, Intense Co, New Brunswick, NJ) and a 760 nm laser (1 W, CrystaLaser LC, Reno, NV). LED modules used to excite fluorescence were fitted with 2 in. diameter short pass filters to reduce the longer wavelength signals that can contaminate fluorescence measurements. Remitted light from the sample is collected using a 500 mm focal distance objective lens (50.8 mm diameter, 400–1100 nm AR coated Achromatic Doublet, Thorlabs, Newton, NJ) and then split into two detection channels; a visible channel and an NIR channel, using a 750 nm short pass dichroic mirror (Thorlabs, Newton, NJ). Light transmitted through the visible detection channel passes through a 10-position high-speed filter wheel (HS1024, FLI, Lima, NY) containing dichroic long pass filters (510 nm and 650 nm used herein) to reduce the excitation signal and a liquid crystal tunable filter (LCTF, Varispec, CRi, Woburn, MA) before being focused on a cooled, 16-bit scientific CMOS camera (Edge 4.2, PCO, Bavaria, Germany). The LCTF enables automated selection of any 7 nm waveband between 420

Biomedical Optics EXPRESS

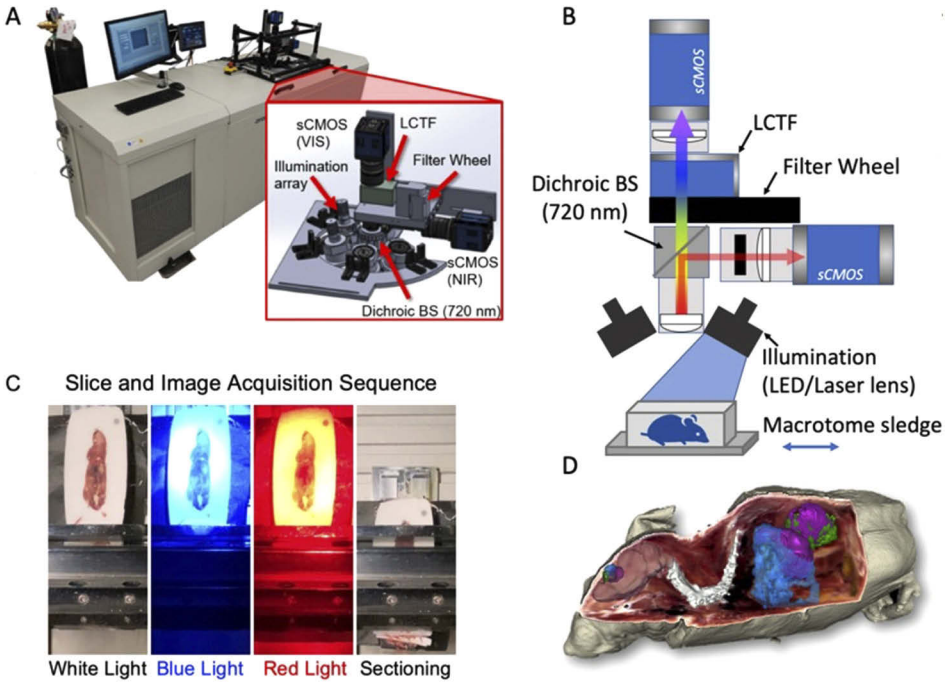


**Fig. 1.** (A) Photograph of the macrotome hyperspectral imaging system with a 3D rendering of the imaging module (inset), (B) schematic diagram for the imaging setup, (C) automated slicing and imaging acquisition sequence and (D) Example of RGB reconstruction and multi-agent fluorescence channel overlays.

and 720 nm, and thus can be used to record hyperspectral image stacks. Light transmitted through the NIR channel is filtered using a long pass filter (herein, a 780 nm cut-on, ThorLabs, Newton, NJ) before detection with a 2nd PCO scientific CMOS camera. The full filter and waveband combination used in this study is presented in Table 1, selected to accommodate the following commonly-used fluorophores: sodium fluorescein (NaFL, Sigma Aldrich, St. Louis, MO, USA), IRDye 680RD and IRDye 800CW (LI-COR Biosciences Inc., Lincoln, NE), and indocyanine green (ICG, Chem-Impex International, Inc., Wood Dale, IL,). In its current configuration, the field of view is 93 × 93 mm and depth of focus 30.5 mm with a lateral resolution of 71 µm or better as determined using a 1951 USAF resolution target.

**Table 1. Excitation and emission configurations for optical channels**

| Light source | Excitation | Emission |
|---|---|---|
| 470 nm LED | 475 nm SP | 510 nm LP/LCTF: 510–720 nm |
| 633 nm laser | None | 650 nm LP/LCTF: 660–720 nm |
| 760 nm laser | None | 780 LP |
| White light | None | LCTF: 420–720 nm |

The automated sectioning/imaging sequence is controlled using custom software written in LabVIEW (National Instruments, Austin, TX, USA). All system parameters (light source selection and intensity, filter combinations, exposure times, etc.) are set and saved in identifiable configuration files prior to imaging to enable ease of use. Once the specimen is positioned, aligned and calibration data acquired, a typical automated acquisition sequence involves:

Biomedical Optics EXPRESS

1. Position filter wheel and turn on white light LED
2. Scan LCTF from 420 nm to 720 nm in preset increments (typically 10 nm). At each waveband, acquire two images, each at different exposure times (typically 10 ms and 50 ms).
3. Turn off LED and acquire dark images.
4. Position filter wheel for the 470 nm LED fluorescence channel, and turn on 470 nm LED
5. Repeat steps 2 and 3 for the 470 nm channel with exposure times of 100 ms and 1000 ms, scanning the LCTF from 510 to 720 nm
6. Repeat steps 3–5 for all additional fluorescence channels
7. Cut section, which removes the top layer based on preset section thickness
8. Repeat steps 1–7 through the entire specimen.

Figure 1(C) shows the specimen during a sampling of the acquisition process (white light illumination, 470 nm illumination, 635 nm illumination, and sectioning). For each light source/waveband combination, we acquire two images at different exposure times to increase the effective dynamic range of the data. Overall, the acquisition process produces multiple hyperspectral image stacks (often hundreds of high-resolution images) per slice. For imaging whole mice, we often section at 100–150 µm per slice, requiring 200–250 slices, thus generating 0.5-1TB of data. All data are written in standard TIFF 16-bit image format directly to a cloud file server to minimize hard drive requirements of the control computer and enable remote image review and data processing during acquisition. An example of a 3-D rendering produced by the instrument is shown in Fig. 1(D).

Total specimen imaging time is determined by the number of fluorescence channels imaged, the number of LCTF wavebands used per channel, the exposure time of each acquisition, the section thickness, the macrotome sectioning time (usually between 20 and 24 s), and thickness of the specimen. In studies for which only RGB and one fluorescence channel are required, total image/sectioning time per slice is typically between 40 and 50 s. Multi-fluorophore imaging with densely-sampled spectra, as performed herein, requires between 3 and 4 m per slice.

### 2.2. Basic image calibration

Each acquired image is accompanied by a dark image with the illumination source extinguished. Basic image processing begins with dark image subtraction followed by exposure time correction. Radial distortion correction is also performed using transformations determined from a checkerboard pattern standard. Before each specimen is imaged, a series of flatfield image stacks were acquired at depths sampled every 1.5 cm in the imaging volume. These images were interpolated to produce a flatfield correction volume which is then applied to the corresponding specimen image stack. This procedure compensates for inhomogeneous illumination fields and serves as a relative intensity correction.

### 2.3. Hyperspectral image stack processing and volume rendering

A typical acquisition sequence results in hyperspectral image stacks of white light reflectance and multiple fluorescent channels at every slice. After the calibration procedure described previously is applied to each image, the hyperspectral stacks are further processed for visualization and analysis.

The white light hyperspectral stack was used for RGB color reconstruction. First, the spectral response of the system was calibrated to the D65 standard illuminant daylight spectrum using hyperspectral images acquired with a color card standard (CameraTrax Inc., Menlo Park, CA, USA). Acquired specimen image stacks were multiplied by wavelength-specific XYZ tristimulus

Biomedical Optics EXPRESS

values using a 1931 CIE standard observer function look-up table (Colour and Vision Laboratory, UCL, London, UK). The XYZ values from each wavelength-specific image were summed to form a composite XYZ image which was then mapped to an RGB 8-bit TIFF image [42]. White balancing was also applied to each RGB channel based on previously calibrated white values.

Hyperspectral image stacks are also acquired for fluorescence emission within the LCTF's wavelength range. These data are processed (per pixel) using the following two approaches: 1) integrating wavebands to recapitulate a standard bandpass filter, heretofore termed "integrated", and 2) applying a spectral unmixing procedure to decouple the specific fluorophore emission from endogenous tissue autofluorescence, or from other fluorophores with overlapping emission spectra. Unmixing is achieved by fitting a combination of pre-recorded basis spectra to the measured data using negatively-constrained linear least-squares fitting, as described previously [38,39] and illustrated in Fig. 2. Specifically, the algorithm applies a Moore-Penrose pseudo-matrix inversion to solve for the relative contributions of pre-recorded basis spectra, $u_i$, using the equation:

$$y(k) = \sum_{i=0}^{N} u_i A_i(\lambda) \tag{1}$$

where $y(\lambda)$ is the measured spectrum, $A_i(\lambda)$ is a matrix composed of $N$ pre-measured basis spectra, and $\lambda$ is wavelength. Since this is repeated at each pixel, the unmixing algorithm is parallelized to accommodate the large volume of data. Currently this processing is applied on a desktop equipped with an Intel Core i7-9800X CPU at 3.8GHz speed with 64 GB RAM and a NVIDIA Quadro P2000 GPU. Unmixed spectra are then integrated to report a single value for each spectral contribution for each pixel.

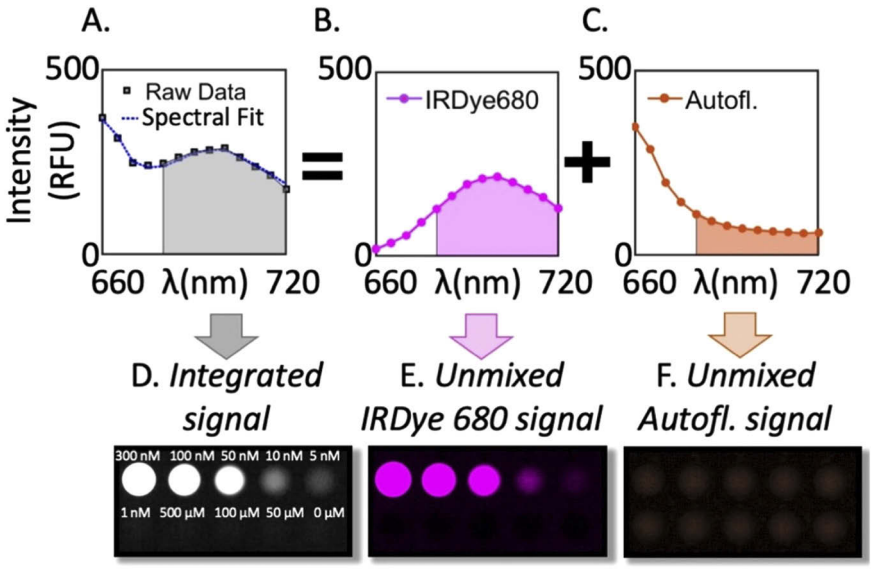


**Fig. 2.** (A) Measured spectrum in one pixel from an intralipid phantom containing 10nM of IRDye680RD carboxylate. Using pre-measured basis spectral, spectral unmixing recovered the relative signal contributions from, (B) the dye and (C) background autofluorescence. The resulting fit is shown with the data in (A). Images of serial dilution phantoms show the integrated signal (no spectral unmixing applied) in (D), and the associated fitted contributions of (E) the dye and (F) autofluorescence.

The resulting data consists of a set of 3-D volumes including; 1) RGB true-color, 2) integrated fluorescence over a pre-defined waveband for each fluorescence channel, and 3) unmixed fluorescence spectra of the constituent fluorophores. These data are then imported into NIRFAST

Biomedical Optics EXPRESS

(Dartmouth College, Hanover, NH and Kitware Inc., Clifton Park, NY, USA), a free image processing software package built on the 3-D Slicer platform (http://www.slicer.org) [43]. Volume visualization, image overlays, segmentation, and quantitative analysis are all completed using this software.

### 2.4. Phantom imaging: fluorophore response linearity and detection limits

Tissue-simulating liquid phantoms were used to evaluate the linearity of response to fluorophore concentration, and determine the minimum detectable concentration. These phantoms consisted of 1% intralipid (Paterson Veterinary Supply, Inc., Greeley, CO, USA) diluted in phosphate-buffered saline and the fluorophore of interest. In this study, we examined: sodium fluorescein (NaFL), IRDye 680RD carboxylate, IRDye 800CW carboxylate, and indocyanine green (ICG). For each fluorescence agent, the concentration was varied from $10^2$ to $10^{-3}$ nM in wells containing 300 µL of solution. For the NaFL and IRDye 680RD carboxylate dyes, hyperspectral stacks were acquired as described in Table 1, and spectrally fit using pre-recorded basis spectra of the dye and phantom autofluorescence. For comparison, we also simulated bandpass filtering with these data, by integrating the emission spectra between 510 and 550 nm for the NaFL channel and between 660 and 700 nm for the IRDye 680 channel.

### 2.5. Animal imaging: multiplexed fluorescent agents in orthotopic glioma xenografts

We examined the biodistribution of three co-administered untargeted flourescent imaging agents in whole animals bearing orthotopic glioma xenografts. All animal experiments were conducted under protocols approved by the Institutional Animal Care and Use Committee at Dartmouth College. Female nude mice (Charles River Laboratories, Wilmington, MD) were inoculated intracranially with $10^6$ U251 glioma cells using procedures described previously [44]. Tumor growth was monitored using gadolinium-enhanced MRI until reaching a size of 2 mm. Animals were then co-administered the fluorescent imaging agents in a 200 µL injection: PEGylated fluorescein (mPEG-FITC, Creative PEGWorks, NC, dosed at 590 nmol), IRDye 680RD conjugated to Affibody Negative Control imaging agent (Abcam plc., Cambridge, MA, USA, dosed at 0.2 nmol) and ICG (dosed at 317 nmol). Animals were euthanized 10 minutes after administration, positioned on a macrotome-compatible sledge, submerged in optimal cutting temperature (OCT) compound (Fisher Scientific, Pittsburgh, PA) and frozen at −20°C for a minimum of eight hours. The frozen specimen block was then mounted on the macrotome sledge and faced in preparation for auto-sectioning and imaging. Tissue autofluorescence basis spectra were acquired using cryo-imaging data of tumor-bearing mice that had not been administered fluorescent agents.

## 3. Results

### 3.1. Linearity of response and detection limit

To quantify the concentration range over which the cryo-imaging system is sensitive, we evaluated the system response to four common fluorophores in serial dilution phantoms covering a range of $10^2$ to $10^{-3}$ nM. The insets in Fig. 3(A-C) show images of the fluorescent phantoms with serial dilutions of NaFL, IRDye680RD carboxylate, and ICG, respectively (IRDye800CW carboxylate images are not shown but display a similar pattern). To quantify the responsivity of the instrument, mean values from each well were computed and plotted as a function of concentration. In the visible channels for which hyperspectral data were acquired (Fig. 3(A and B)), both the integrated and spectrally unmixed measurements were computed and plotted. As shown in the graphs, spectral unmixing consistently reduced the limit of detection compared to the integrated spectra data.

In all cases, the lowest concentration values were used to establish the sensitivity limit for that channel, and the linearity of all data above this limit computed. The minimum detectable

Biomedical Optics EXPRESS

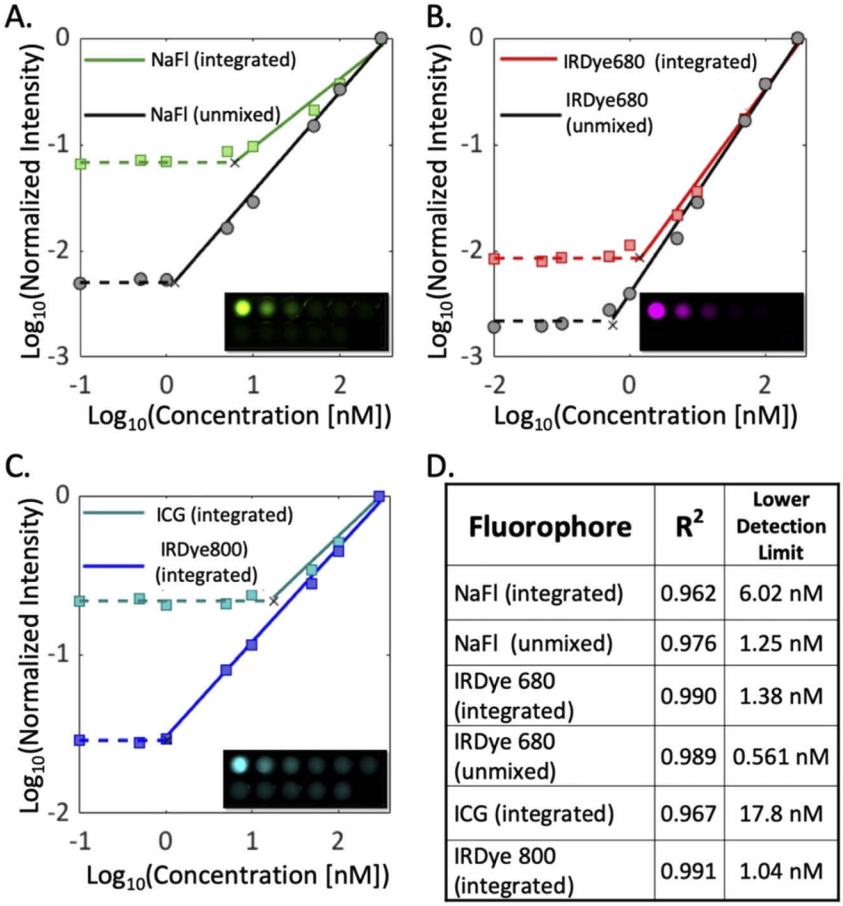


| Fluorophore | $R^2$ | Lower Detection Limit |
|---|---|---|
| NaFl (integrated) | 0.962 | 6.02 nM |
| NaFl (unmixed) | 0.976 | 1.25 nM |
| IRDye 680 (integrated) | 0.990 | 1.38 nM |
| IRDye 680 (unmixed) | 0.989 | 0.561 nM |
| ICG (integrated) | 0.967 | 17.8 nM |
| IRDye 800 (integrated) | 0.991 | 1.04 nM |

**Fig. 3.** The linearity of response to fluorophore concentration of the imaging cryo-macrotome for four fluorophores in intralipid phantoms: (A) NaFL showing both integrated and spectrally unmixed results, (B) LI-COR IRDye 680RD showing both integrated and spectrally unmixed results, and (C) NIR channel measurements of ICG and LI-COR IRDye 800CW carboxylate (acquired separately, no spectral unmixing). (D) provides the lowest detectable concentration for each channel/processing approach.

concentrations for each fluorophore are provided in Fig. 3(D). With the exception of ICG, the limit of detection for each dye was around 1 nM. Spectral fitting conferred significant improvements in detectability: by a factor of 4.8 for NaFL and 2.5 for IRDye680. Of all the dyes, the instrument was most sensitive to the IRDye680, achieving sub-nM sensitivity.

### *3.2. Imaging multiple fluorophores in whole animals*

We examined the capacity of hyperspectral cryo-imaging to report the biodistribution of three co-administered fluorescent agents in mice bearing orthotopic glioma xenografts. Figure 4(A-D) shows representative images of one slice for all four channels: (A) a white light image, (B) mPEG-FITC, (C) IRDye 680 Affibody NC, and (D) ICG. These images have undergone basic calibration described in Section 2.2, and images from the visible fluorescence channels (B and C) are of the integrated emission spectra (not spectrally-unmixed). As is evident from these 2-D slices, each untargeted agent displays a distinct biodistribution behavior.

Biomedical Optics EXPRESS

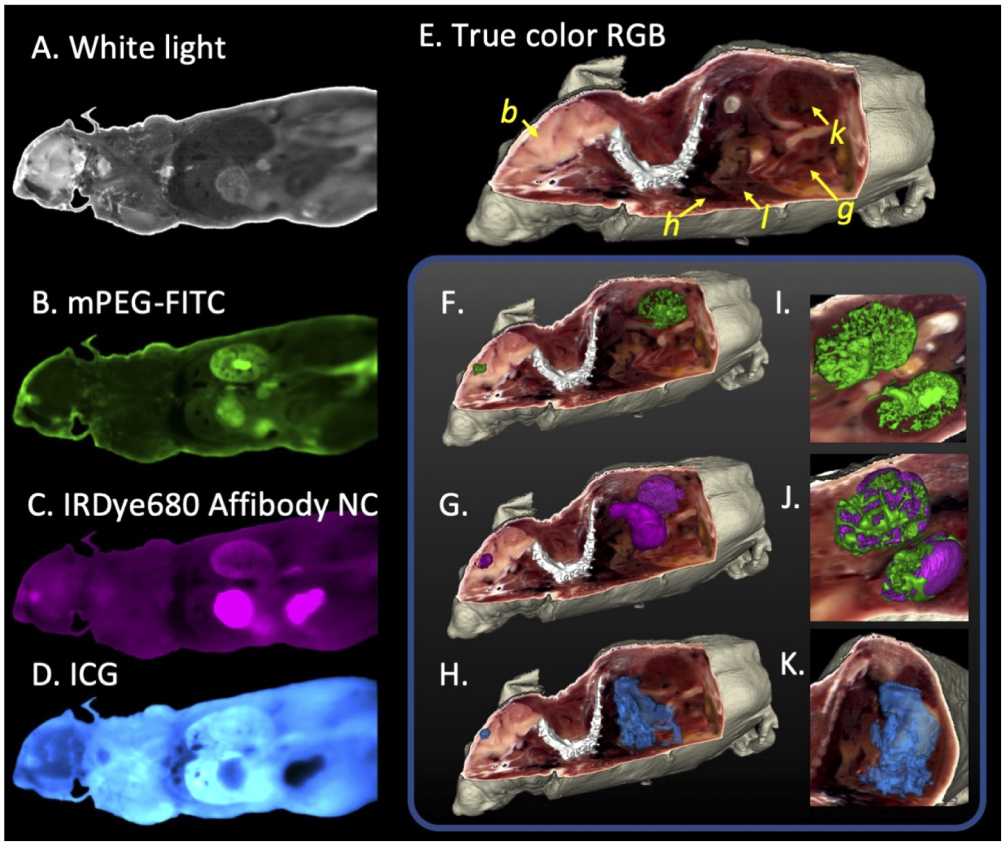


**Fig. 4.** Representative single slice cryoimages of four channels (not spectrally unmixed) in one mouse: (A) white light, (B) mPEG-FITC; (C) IRDye680 Affibody NC; and (D) ICG. (E) Reconstructed true color anatomic rendering with several organs labeled: brain *(b)*, heart (h), liver *(l)*, kidney *(k)*, and the gastrointestinal system (*g*). True color with fluorescence channel overlay renderings of mPEG-FITC (F), IRDye680 Affibody NC (G), and ICG (H). Magnified images of the distribution of mPEG-FITC (I) and IRDye680 Affibody NC (J) in the kidneys, and ICG agent distribution in the liver region (K).

Biomedical Optics EXPRESS

Figure 4(E) shows a rendering of the RGB image volume (with orthogonal clipping) recovered from the hyperspectral white light reflectance data using the RGB remixing algorithm described in Section 2.3, and Fig. 4(F-H) shows the corresponding fluorescence data rendered and overlaid on the RGB volume. The distinct uptake patterns between the three agents in the tumor and excretion organs are evident. Excretion of mPEG-FITC and IRDye680-NC at this time point appears to be primarily through the kidneys, yet these agents show distinct patterns in this organ, while ICG excretion is observed primarily in the liver. Tumor distribution also varies widely between the agents at this time point.

Figure 5 illustrates the spectral unmixing process for the 635 nm (IRDye680-NC) channel. Figure 5(A) represents the hyperspectral image data stack for one slice, which here consists of seven images of the same slice, each at a different waveband. The spectral unmixing algorithm is applied at each image pixel, using three basis spectra: (1) dye fluorescence, (2) normal brain autofluorescence and (3) necrotic tissue autofluorescence. The spectral data, fitted result, and constituent basis spectra for two different image pixels are shown in Fig. 5(B) and (C). In this case the region of highest fluorescence intensity consisted primarily of necrotic autofluorescence,

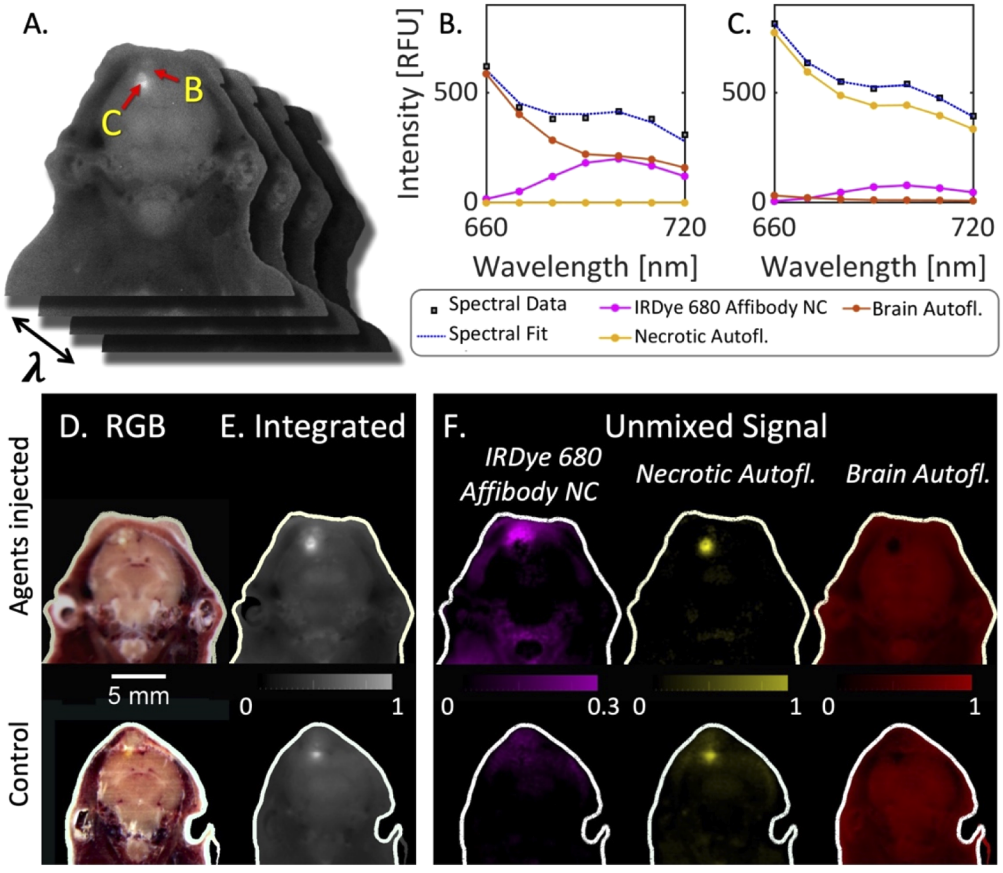


**Fig. 5.** (A) Illustration of a hyperspectral image stack acquired with the red excitation channel. (B) and (C) are spectra sampled at two different pixels, one in necrotic tissue (B) and the other in surrounding tumor (C). (D) Single RGB image slice of two mice, one administered the agents, and a non-injected control. (E) Images of the integrated red channel spectrum. (F) Images of the contribution of each basis spectra after spectral unmixing in both the injected and control mice. Both animals had an orthotopic glioma xenograft.

Biomedical Optics EXPRESS

not dye fluorescence. Figure 5(D-F) show the results of spectral unmixing for one slice of data in two tumor-bearing animals: one administered the imaging agent cocktail, and a control animal that had not received the imaging agents. The column labeled (D) provides the results if only a bandpass filter were to be used, and indicates that the highest fluorescence intensity is in the necrotic region of the tumor, regardless of whether dye had been injected. Panel (F) provides the resulting spectrally unmixed images (integrated basis spectra after unmixing). Notably, the distribution of the contrast agent in the injected mouse is altered significantly as fluorescence from the necrotic region, which would have otherwise been attributed to the dye, is properly classified. This is further illustrated in the control animal which showed significant signal in the integrated images, the origin of which could not be determined without unmixing.

A closer examination of the brain demonstrates the potential influence of spectral unmixing on image interpretation in the visible channels. Figure 6 shows 2-D slices (A and B) and renderings (C) of all three administered agents. For the visible channels (mPEG-FITC and IRDye680-NC), integrated spectra are shown in (A), spectrally unmixed data in (B), and examples of FITC spectral unmixing results in two pixels provided in (D) and (E). Without hyperspectral imaging in the NIR channel, the ICG data are inherently integrated. Within the integrated data, the mPEG-FITC agent produced the highest tumor-to-normal contrast, and substantial signal from the normal

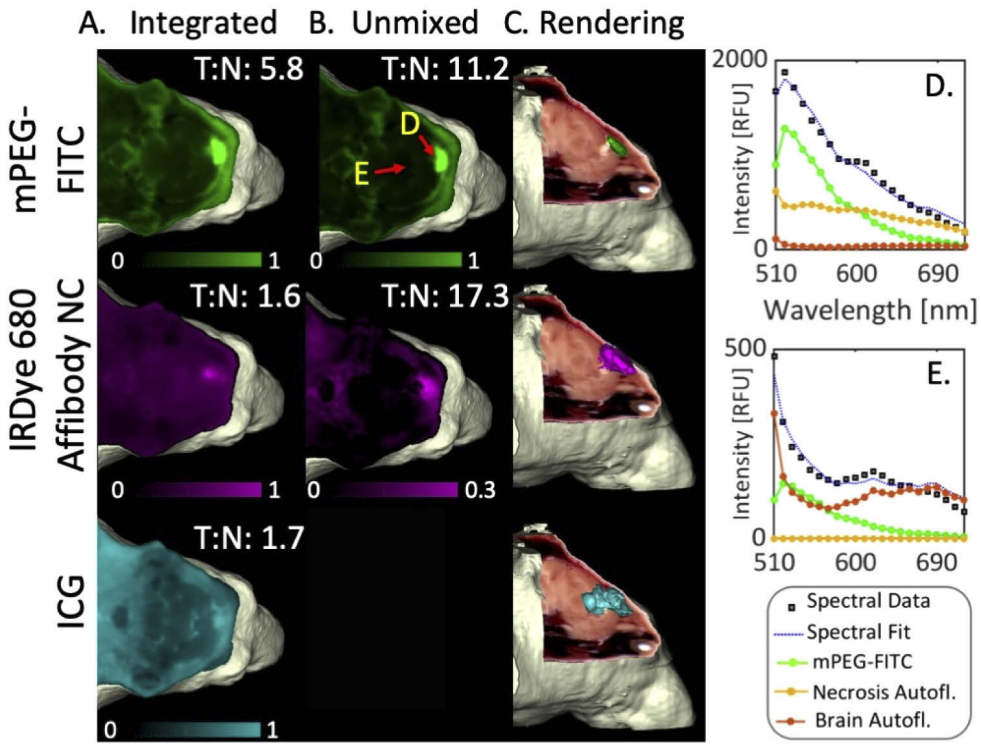


**Fig. 6.** (A) Integrated signal (one slice) for all three fluorescence channels: mPEG-FITC, unmixed IRDye 680 Affibody NC, and ICG. Spectrally unmixed signal for mPEG-FITC and IRDye 680 are shown in (B), and renderings of segmented agent distribution observed in the unmixed mPEG-FITC channel, unmixed IRDye 680 Affibody NC channel, and integrated ICG channel are provided in (C). (D) and (E) show measured spectra, spectral fits, and the relative contributions of all basis spectra in two representative pixels in the FITC channel (indicated by arrows in B). Tumor-to-normal contrasts are provided in 2-D image panels as T:N.

Biomedical Optics EXPRESS

tissue was observed for the other two agents, especially ICG. Qualitative assessment of the visible channel data exclusively reveals significant differences in the spatial distribution of agent between the integrated and unmixed images. In both FITC and IRDye680 channels, spectral unmixing reduced the signal in the normal brain and in the necrotic region of the tumor. Quantitative analysis shows a significant increase in tumor-to-normal contrast after spectral unmixing in this representative example. To further evaluate the potential improvement in tumor-to-normal contrast, we imaged eight glioma-bearing animals using the mPEG-FITC dye and completed a paired analysis comparison between integrated and spectrally-unmixed tumor-to-normal contrast. On average, spectral fitting increased contrast by a factor of 1.54, and the difference between the integrated and spectrally unmixed contrast was statistically significant ($p < 0.03$ using a paired-sample two-tailed Student's t-test).

## 4. Discussion and conclusion

Herein, we report on hyperspectral fluorescence imaging and spectral unmixing applied to whole animal cryo-imaging. Although this methodology has been deployed in a variety of other applications, including imaging of living small animals [36,37], surgical guidance [40,41,45], microscopy [46–48], tomographic imaging [38,49] and clinical point probe measurements [50,51], all demonstrating improvements in the ability to isolate the specific signal-of-interest, this study is the first to evaluate the technique in whole body cryo-imaging. In this configuration, the hyperspectral information reduced the detection limit thresholds by 2–5 times, which can be important for applications in which reporter signal is relatively low compared to other contaminating signals.

Notably, applying hyperspectral unmixing in a glioma model significantly altered the interpretation of the agent biodistribution. Spectral unmixing reduced the influence of endogenous signal in the normal brain, increasing tumor-to-background contrast by a factor of 10 in the IRDye680-NC channel and 2 in the FITC channel. Additionally, the necrotic region of these tumors showed substantial autofluorescence in the visible wavebands, which contaminated the fluorescence signal of both visible fluorophores. Without the spectral information, these regions were incorrectly attributed to agent accumulation, yet the unmixing process showed that the agent accumulated primarily around the necrotic region. The ability to isolate the agent to provide an accurate rendering of biodistribution would have important implications for examining drug distribution or assessing new fluorescent contrast agents.

The spectral unmixing approach is most beneficial when the contaminating signals (such as autofluorescence) are spectrally distinct, measurable *a priori*, and on the same order as the signal emitted by the reporter. For cases in which the reporter signal is substantially higher than the endogenous signal, spectral unmixing may only confer a modest quantitative benefit. Similarly, the approach will not reliably quantify reporter fluorescence in cases for which the background signal is orders higher than the reporter's, though non-spectrally-resolved data would also be unreliable in these cases. Visible fluorescence imaging in the gut is particularly challenging as autofluorescence intensity is often very high in these regions, even when animals are on low-chlorophyll diets. Ultimately, the utility of imaging in this region will be contingent on a relatively strong signal from the reporter and/or distance from autofluorescing organs.

As applied herein, the autofluorescence basis spectra were assumed to be known explicitly and were catalogued from animals that had not been administered optical contrast agents. This is fairly straightforward for narrowly-defined regions of the animal, such as the head of the mouse, as examined herein. Applying the method throughout an entire animal is more challenging as the number of autofluorescence sources, and thus basis spectra increase. This facilitates a risk of data overfitting unless additional spatial or spectral constraints are applied. Optimizing this procedure is a focus of ongoing work in our lab. Additionally, the appearance of fluorescent sources that are not characterized *a priori* could lead to inaccurate estimations of fluorophore

Biomedical Optics EXPRESS

activity. Yet, the presence of a confounding signal may be identified through inspection of the measured spectrum and/or spectral fitting quality metrics, a capability not available with imaging systems employing conventional bandpass filtering.

The hyperspectral whole animal cryo-imaging approach reported here is broadly applicable to most of the fluorophores used in clinical and preclinical research. The methodology uses established hyperspectral processing techniques to improve image accuracy and enable a high level of reporter multiplexing to examine multiple processes in one animal. This capability could play a central role in developing novel optical contrast agents, studying drug distribution and pharmacological effects, and monitoring metastatic spread.

## Funding

National Cancer Institute (R01CA184354, R01CA188491); Norris Cotton Cancer Center (SYNERGY Translational Pilot Grant).

## Disclosures

The authors declare no conflicts of interest.

## References

1. J. W. McLean, E. A. Fox, P. Baluk, P. B. Bolton, A. Haskell, R. Pearlman, G. Thurston, E. Y. Umemoto, and D. M. McDonald, "Organ-specific endothelial cell uptake of cationic liposome-DNA complexes in mice," Am. J. Physiol-Heart C. **273**(1), H387–H404 (1997).
2. H. E. Daldrup-Link, M. Rudelius, S. Metz, G. Piontek, B. Pichler, M. Settles, U. Heinzmann, J. Schlegel, R. A. J. Oostendorp, and E. J. Rummeny, "Cell tracking with gadophrin-2: a bifunctional contrast agent for MR imaging, optical imaging, and fluorescence microscopy," Eur. J. Nucl. Med. Mol. Imaging **31**(9), 1312–1321 (2004).
3. F. Gamarra, S. Wagner, S. Al-Batran, I. Maier, M. Castro, H. Hautmann, A. Bergner, R. Baumgartner, and R. M. Huber, "Kinetics of 5-Aminolevulinic Acid-Induced Fluorescence in Organ Cultures of Bronchial Epithelium and Tumor," Respiration **69**(5), 445–450 (2002).
4. H. Dafni, L. Landsman, B. Schechter, F. Kohen, and M. Neeman, "MRI and fluorescence microscopy of the acute vascular response to VEGF165: vasodilation, hyper-permeability and lymphatic uptake, followed by rapid inactivation of the growth factor," NMR Biomed. **15**(2), 120–131 (2002).
5. E. Caussinus, O. Kanca, and M. Affolter, "Fluorescent fusion protein knockout mediated by anti-GFP nanobody," Nat. Struct. Mol. Biol. **19**(1), 117–121 (2012).
6. M. J. Moreno, B. Ling, and D. B. Stanimirovic, "In vivo near-infrared fluorescent optical imaging for CNS drug discovery," Expert Opin. Drug Discovery **15**(8), 903–915 (2020).
7. F. Helmchen and W. Denk, "New developments in multiphoton microscopy," Curr. Opin. Neurobiol. **12**(5), 593–601 (2002).
8. F. Leblond, S. C. Davis, P. A. Valdes, and B. W. Pogue, "Pre-clinical whole-body fluorescence imaging: review of instruments, methods and applications," J. Photochem. Photobiol., B **98**(1), 77–94 (2010).
9. T. Etrych, H. Lucas, O. Janoušková, P. Chytil, T. Mueller, and K. Mäder, "Fluorescence optical imaging in anticancer drug delivery," J. Controlled Release **226**, 168–181 (2016).
10. F. Helmchen and W. Denk, "Deep tissue two-photon microscopy," Nat. Methods **2**(12), 932–940 (2005).
11. M. D. Cahalan, I. Parker, S. H. Wei, and M. J. Miller, "Real-time imaging of lymphocytes in vivo," Curr. Opin. Immunol. **15**(4), 372–377 (2003).
12. P. Bousso and E. A. Robey, "Dynamic behavior of T cells and thymocytes in lymphoid organs as revealed by two-photon microscopy," Immunity **21**(3), 349–355 (2004).
13. N. L. Garrett, A. Lalatsa, I. Uchegbu, A. Schätzlein, and J. Moger, "Exploring uptake mechanisms of oral nanomedicines using multimodal nonlinear optical microscopy," J. Biophoton. **5**(5-6), 458–468 (2012).
14. B. A. Molitoris and R. M. Sandoval, "Intravital multiphoton microscopy of dynamic renal processes," Am. J. Physiol. Renal Physiol. **288**(6), F1084–F1089 (2005).
15. M. Rubart, "Two-photon microscopy of cells and tissue," Circ. Res. **95**(12), 1154–1166 (2004).
16. J. J. Kelly, J. R. Ewen, S. L. Bernard, R. W. Glenny, and C. H. Barlow, "Regional blood flow measurements from fluorescent microsphere images using an Imaging CryoMicrotome," Rev. Sci. Instrum. **71**(1), 228–234 (2000).
17. S. L. Bernard, J. R. Ewen, C. H. Barlow, J. J. Kelly, S. McKinney, D. A. Frazer, and R. W. Glenny, "High spatial resolution measurements of organ blood flow in small laboratory animals," Am. J. Physiol-Heart C. **279**(5), H2043–H2052 (2000).
18. D. Wilson, D. Roy, G. Steyer, M. Gargesha, M. Stone, and E. McKinley, "Whole mouse cryo-imaging," in Medical Imaging 2008: Physiology, Function, and Structure from Medical Images (International Society for Optics and Photonics, 2008), 6916, p. 69161I.

Biomedical Optics EXPRESS


19. D. Roy, G. J. Steyer, M. Gargesha, M. E. Stone, and D. L. Wilson, "3D cryo-imaging: a very high-resolution view of the whole mouse," Anat. Rec. **292**(3), 342–351 (2009).
20. D. Roy, M. Gargesha, G. J. Steyer, P. Hakimi, R. W. Hanson, and D. L. Wilson, "Multi-Scale Characterization of the PEPCK- C mus Mouse through 3D Cryo-Imaging," Int. J. Biomed. Imaging **2010**(2010), 1–11 (2010).
21. J. P. H. M. van den Wijngaard, J. C. V. Schwarz, P. van Horssen, M. G. J. T. B. van Lier, J. G. G. Dobbe, J. A. E. Spaan, and M. Siebes, "3D Imaging of vascular networks for biophysical modeling of perfusion distribution within the heart," J. Biomech. **46**(2), 229–239 (2013).
22. A. Sarantopoulos, G. Themelis, and V. Ntziachristos, "Imaging the bio-distribution of fluorescent probes using multispectral epi-illumination cryoslicing imaging," Mol. Imaging Biol. **13**(5), 874–885 (2011).
23. G. J. Steyer, D. Roy, O. Salvado, M. E. Stone, and D. L. Wilson, "Cryo-imaging of fluorescently labeled single cells in a mouse," in Medical Imaging 2009: Biomedical Applications in Molecular, Structural, and Functional Imaging (International Society for Optics and Photonics, 2009), 7262, p. 72620W.
24. P. Wuttisarnwattana, M. Gargesha, W. van't Hof, K. R. Cooke, and D. L. Wilson, "Automatic stem cell detection in microscopic whole mouse cryo-imaging," IEEE Trans. Med. Imaging **35**(3), 819–829 (2016).
25. M. Q. Qutaish, K. E. Sullivant, S. M. Burden-Gulley, H. Lu, D. Roy, J. Wang, J. P. Basilion, S. M. Brady-Kalnay, and D. L. Wilson, "Cryo-image analysis of tumor cell migration, invasion, and dispersal in a mouse xenograft model of human glioblastoma multiforme," Mol. Imaging Biol. **14**(5), 572–583 (2012).
26. Z. Zhou, M. Qutaish, Z. Han, R. M. Schur, Y. Liu, D. L. Wilson, and Z.-R. Lu, "MRI detection of breast cancer micrometastases with a fibronectin-targeting contrast agent," Nat. Commun. **6**(1), 7984 (2015).
27. M. Q. Qutaish, Z. Zhou, D. Prabhu, Y. Liu, M. R. Busso, D. Izadnegahdar, M. Gargesha, H. Lu, Z.-R. Lu, and D. L. Wilson, "Cryo-imaging and software platform for analysis of molecular MR Imaging of micrometastases," Int. J. Biomed. Imaging **2018**(2018), 1–16 (2018).
28. P. van Horssen, M. Siebes, I. Hoefer, J. A. E. Spaan, and J. P. H. M. van den Wijngaard, "Improved detection of fluorescently labeled microspheres and vessel architecture with an imaging cryomicrotome," Med. Biol. Eng. Comput. **48**(8), 735–744 (2010).
29. P. Symvoulidis, C. C. Perez, M. Schwaiger, V. Ntziachristos, and G. G. Westmeyer, "Serial sectioning and multispectral imaging system for versatile biomedical applications," in *2014 IEEE 11th International Symposium on Biomedical Imaging (ISBI)* (IEEE, 2014), pp. 890–893.
30. Y. Inoue, K. Izawa, S. Kiryu, A. Tojo, and K. Ohtomo, "Diet and abdominal autofluorescence detected by in vivo fluorescence imaging of living mice," Mol. Imaging **7**(1), 7290 (2008).
31. T. Troy, D. Jekic-McMullen, L. Sambucetti, and B. Rice, "Quantitative comparison of the sensitivity of detection of fluorescent and bioluminescent reporters in animal models," Mol. Imaging **3**(1), 153535002004031 (2004).
32. S. Andersson-Engels, J. Johansson, U. Stenram, K. Svanberg, and S. Svanberg, "Malignant tumor and atherosclerotic plaque diagnosis using laser-induced fluorescence," IEEE J. Quantum Electron. **26**(12), 2207–2217 (1990).
33. R. Cubeddu, G. Canti, P. Taroni, and G. Valentini, "Time-gated fluorescence imaging for the diagnosis of tumors in a murine model," Photochem. Photobiol. **57**(3), 480–485 (1993).
34. L. Gu, D. J. Hall, Z. Qin, E. Anglin, J. Joo, D. J. Mooney, S. B. Howell, and M. J. Sailor, "In vivo time-gated fluorescence imaging with biodegradable luminescent porous silicon nanoparticles," Nat. Commun. **4**(1), 2326 (2013).
35. D. L. Farkas, C. Du, G. W. Fisher, C. Lau, W. Niu, E. S. Wachman, and R. M. Levenson, "Non-invasive image acquisition and advanced processing in optical bioimaging," Comput. Med. Imaging Graph. **22**(2), 89–102 (1998).
36. J. R. Mansfield, K. W. Gossage, C. C. Hoyt, and R. M. Levenson, "Autofluorescence removal, multiplexing, and automated analysis methods for in-vivo fluorescence imaging," J. Biomed. Opt. **10**(4), 041207 (2005).
37. R. M. Levenson and J. R. Mansfield, "Multispectral imaging in biology and medicine: Slices of life," Cytometry **69A**(8), 748–758 (2006).
38. S. C. Davis, B. W. Pogue, R. Springett, C. Leussler, P. Mazurkewitz, S. B. Tuttle, S. L. Gibbs-Strauss, S. S. Jiang, H. Dehghani, and K. D. Paulsen, "Magnetic resonance-coupled fluorescence tomography scanner for molecular imaging of tissue," Rev. Sci. Instrum. **79**(6), 064302 (2008).
39. B. Meng, M. R. Folaron, B. K. Byrd, K. S. Samkoe, R. S. Strawbridge, C. Barth, S. L. Gibbs, and S. C. Davis, "Topical dual-probe staining using quantum dot-labeled antibodies for identifying tumor biomarkers in fresh specimens," PLoS One **15**(3), e0230267 (2020).
40. J. J. Bravo, J. D. Olson, S. C. Davis, D. W. Roberts, K. D. Paulsen, and S. C. Kanick, "Hyperspectral data processing improves PpIX contrast during fluorescence guided surgery of human brain tumors," Sci. Rep. **7**(1), 9455 (2017).
41. P. A. Valdes, V. L. Jacobs, B. C. Wilson, F. Leblond, D. W. Roberts, and K. D. Paulsen, "System and methods for wide-field quantitative fluorescence imaging during neurosurgery," Opt. Lett. **38**(15), 2786 (2013).
42. E. Reinhard, E. A. Khan, A. O. Akyuz, and G. Johnson, *Color Imaging: Fundamentals and Applications* (CRC Press, 2008).
43. A. Federov, R. Beichel, J. Kalpathy-Cramer, J. Finet, J. C. Fillion-Robin, S. Pujol, C. Bauer, D. Jennings, M. Fennessy, D. Jennings, M. Sonka, J. Buatti, S. Aylward, J. V. Miller, S. Pieper, and R. Kikinis, "3D Slicer as an image computing platform for the Quantitative Imaging Network," Magnetic Resonance Imaging **30**(9), 1323–1341 (2012).
44. K. S. Samkoe, S. L. Gibbs-Strauss, H. H. Yang, S. Khan Hekmatyar, P. Jack Hoopes, J. A. O'Hara, R. A. Kauppinen, and B. W. Pogue, "Protoporphyrin IX fluorescence contrast in invasive glioblastomas is linearly correlated with Gd

Biomedical Optics EXPRESS

enhanced magnetic resonance image contrast but has higher diagnostic accuracy," J. Biomed. Opt. **16**(9), 096008 (2011).
45. A. D. Elliott, L. Gao, A. Ustione, N. Bedard, R. Kester, D. W. Piston, and T. S. Tkaczyk, "Real-time hyperspectral fluorescence imaging of pancreatic -cell dynamics with the image mapping spectrometer," J. Cell Sci. **125**(20), 4833–4840 (2012).
46. M. E. Dickinson, G. Bearman, S. Tille, R. Lansford, and S. E. Fraser, "Multi-spectral imaging and linear unmixing add a whole new dimension to laser scanning fluorescence microscopy," BioTechniques **31**(6), 1272–1278 (2001).
47. T. Zimmermann, J. Rietdorf, and R. Pepperkok, "Spectral imaging and its applications in live cell microscopy," FEBS Lett. **546**(1), 87–92 (2003).
48. T. C. Rich, A. L. Britain, T. Stedman, and S. J. Leavesley, "Hyperspectral imaging of FRET-based cGMP probes," in Guanylate Cyclase and Cyclic GMP, T. Krieg and R. Lukowski, eds., Methods in Molecular Biology (Humana Press, 2013), 1020, pp. 73–88.
49. G. Zacharakis, R. Favicchio, M. Simantiraki, and J. Ripoll, "Spectroscopic detection improves multi-color quantification in fluorescence tomography," Biomed. Opt. Express **2**(3), 431–439 (2011).
50. S. C. Kanick, S. C. Davis, Y. Zhao, T. Hasan, E. V. Maytin, B. W. Pogue, and M. S. Chapman, "Dual-channel red/blue fluorescence dosimetry with broadband reflectance spectroscopic correction measures protoporphyrin IX production during photodynamic therapy of actinic keratosis," J. Biomed. Opt. **19**(7), 075002 (2014).
51. P. A. Valdés, F. Leblond, A. Kim, B. C. Wilson, K. D. Paulsen, and D. W. Roberts, "A spectrally constrained dual-band normalization technique for protoporphyrin IX quantification in fluorescence-guided surgery," Opt. Lett. **37**(11), 1817 (2012).